Underactuated fluidic control of a continuous multistable membrane

Ofek Peretz[a,1], Anand K. Mishra[b], Robert F. Shepherd[b], and Amir D. Gat[a]

[a]Faculty of Mechanical Engineering, Technion–Israel Institute of Technology, Haifa 3200003, Israel; and [b]Department of Mechanical and Aerospace Engineering, Cornell University, Ithaca, NY 14853

Edited by John A. Rogers, Northwestern University, Evanston, IL, and approved January 29, 2020 (received for review November 12, 2019)

This work addresses the challenge of underactuated pattern generation in continuous multistable structures. The examined configuration is a slender membrane which can concurrently sustain two different equilibria states, separated by transition regions, and is actuated by a viscous fluid. We first demonstrate the formation and motion of a single transition region and then sequencing of several such moving transition regions to achieve arbitrary patterns by controlling the inlet pressure of the actuating fluid. Finally, we show that nonuniform membrane properties, along with transient dynamics of the fluid, can be leveraged to directly snap through any segment of the membrane.

viscous flow | bistability | multistability | soft actuators | soft robotics

A bistable or a multistable elastic element is a structure capable of transforming between different equilibrium deformation patterns, due to the stability transitions of its characteristic energy profile (Fig. 1) (1, 2). Bistable elements, such as curved elastic membranes, which exhibit snapping instabilities, are becoming increasingly popular in the design of switches and actuators in microelectromechanical systems (MEMS), for designing mechanical logic systems, origami structures, and energy-efficient soft robots (3–5). A common way to fabricate such a system is by combining multiple discrete bistable elements, yielding the entire configuration as a multistable structure.

Pressurization of confined fluids is a leading method for the actuation of such bistable elements, yielding governing dynamics involving both viscous and elastic effects. While the interaction of fluids bounded by elastic structures was extensively studied in recent years (refs. 6–12, as well as discussion in ref. 13), only a few researchers examined viscous flow interacting with bistable elasticity (e.g., refs. 14–18). Previous relevant works involving bistability and viscous flow include the work by Hazel and Heil (19), who numerically studied the steady flow of a viscous fluid through a thin-walled elastic tube connected to two rigid tubes. When the pressure acting on the tube's shell surpasses a critical value, the tube buckles and strongly modifies fluidic flow within the tube. Another recent relevant work by Gomez et al. (17) demonstrated passive control of viscous flow in a channel via an elastic arc positioned within the channel. By controlling the volumetric fluid flux, the bistable elastic arc can be made to snap between two deformation patterns, therefore modifying the channel's viscous resistance by order of magnitude. Thus, the authors showed that bistability could be effectively used to replace externally controlled valves. Arena et al. (20) recently introduced a conceptual design for adaptive structures that utilize the instabilities of postbuckled membranes to obtain flow regulation and control. By tailoring the stress field in the postbuckled state and the geometry of the initial, stress-free configuration, the deformable section can snap through to close or open the inlet completely, thus providing a self-stimulating actuator that regulates the inlet flow without requiring external flow-regulating mechanisms.

So far, all previous works examined the actuation dynamics of either a single bistable element (21, 22) or multistable structures (23–27), which are an assembly of discrete bistable elements. In this work, we present analysis and demonstration of fluidic control of a continuous, multistable structure. In contrast with discrete multistable configurations, such continuous structures inherently have infinite possible stable patterns. Importantly, in many of these works, each element has its own control input for inducing transitions between its bistable states (28, 29). Therefore, generating complex deformation patterns of such a multistable structure typically requires control of multiple inputs, which greatly complicates the system's operation. We thus focus on achieving underactuated fluidic control, enabling to arbitrarily pattern such continuous structures by a single pressure inlet.

The configuration studied in this work is presented in Fig. 2, showing the experimental setup, including the membrane and a transition region separating between the two different equilibria states. The x coordinate denotes the streamwise direction, where the inlet is located at $x=0$. The location of the transition region is denoted by $x_s^-(t)<x<x_s^+(t)$. Initially, the entire membrane is at the snapped-up state. A sudden decrease in inlet pressure initiates snap-down near the inlet (Fig. 2, region 1). A transition region (Fig. 2, region 2) then starts propagating, separating the snapped-down region from the membrane segment, which remained at the initial snapped-up state (Fig. 2, region 3). To achieve two stable equilibria states at rest (meaning fluidic gauge pressure $p=0$), we require both $p_s^{down}<0$ and $p_s^{up}>0$.

Significance

Mechanical elements which exhibit several equilibria states and snapping instabilities are increasingly popular in the design of microelectromechanical systems, mechanical logic systems, origami structures, and especially in soft robotics. All previous research examined the actuation dynamics of either a single bistable element or multistable structures, which are an assembly of discrete bistable elements. In this work, we present analysis and experimental demonstration of underactuated fluidic control of a continuous multistable structure, enabling us to arbitrarily pattern such continuous structures by a single pressure inlet. These continuous multistable structures inherently have infinite possible stable patterns, thus offering an essential increase in versatility.

Author contributions: O.P., R.F.S., and A.D.G. designed research; O.P. and A.K.M. performed research; O.P. contributed new reagents/analytic tools; O.P. analyzed data; and O.P. and A.D.G. wrote the paper.

The authors declare no competing interest.

This article is a PNAS Direct Submission.

Published under the PNAS license.

Data deposition: Related codes used in the work are available at Figshare (https://doi.org/10.6084/m9.figshare.11648022.v1).

[1]To whom correspondence may be addressed. Email: ofekperetz@campus.technion.ac.il.

This article contains supporting information online at https://www.pnas.org/lookup/suppl/doi:10.1073/pnas.1919738117/-/DCSupplemental.

Downloaded at Eyachar Central Lib Technion - Israel Inst of Tech on February 25, 2020

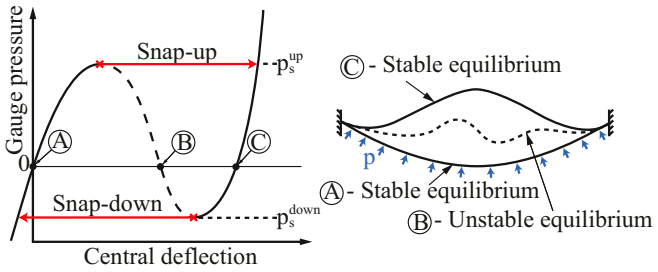

Fig. 1. An illustration of a bistable behavior of a clamped–clamped curved elastic membrane. At the initial state (A), the configuration is at a stable deformation pattern. When pressure is applied on the bottom surface of the membrane, the component deforms gradually until a critical value of the pressure (denoted by p_s^{up}). At this point, the component snaps through a region of unstable deformation shapes (B) until reaching a second stable deformation pattern (C). At state (C), decreasing the pressure below p_s^{up} will not bring the membrane back to state (A), due to hysteresis effect of the bistable dynamics. Snapping back to state (A) requires reaching a different lower critical value (denoted by p_s^{down}), associated with state (C).

The experimental setup consists of a rectangular channel, a pressure-flow controller, and a viscous fluid reservoir (Fig. 2). We used a rigid material for the side and bottom walls [poly(methyl methacrylate)] and soft membrane (latex) for the top wall. The dimensions of the fabricated channel were 16.6 × 15.8 × 800 mm (width × height × length), and the soft membrane was 35 mm wide and 0.52 mm thick, with an elastic modulus of E = 100 MPa. To obtain a geometric bistability, we clamped the 35-mm-wide membrane onto the shorter 15.8-mm-wide channel (Fig. 2). This created two stable deformation states, with centerline heights of 29.6 and 2.05 mm for the snapped-up and -down states. We connected the channel to a pressure controller (Elveflow OB1) at the inlet (at x = 0 mm) and kept the outlet (at x = 800 mm) open to atmospheric pressure. To actuate the channel, we used glycerol as a viscous fluid (ρ = 1.26 g/cm^3 and viscosity of μ = 1.412 Pa·s). The snapping pressures (definitions in Fig. 1) were experimentally measured as p_s^{up} = 5 kPa for snapped-up and p_s^{down} = −5 kPa for the snapped-down state, with SD of ±0.13 kPa for both states. The measurements were based on averaging six experiments and used air actuation to ensure elimination of transient fluidic effects.

Using this setup, in Fig. 3, we demonstrate the propagation of a single transition region in the channel. The initial state of the membrane is at a snapped-up state, and then we apply a Heaviside inlet pressure function of p_{in} = −10 kPa at $t = 0$ s. The negative inlet pressure creates transition to snap-down near the inlet as well as a transition region separating the snapped-up state far from the inlet. As time progresses, the transition region propagates along the flow direction, and the membrane gradually changes its state from snapped-up to snapped-down. The shape of the membrane at different time intervals is presented in Fig. 3, where the blue and black lines represent the theoretical (derivation below) and experimental location of the transition region x_s vs. time t. We also report a characteristic length of the transition region of ≈4 channel widths, thus yielding a ratio between the transition region length and the channel length of 0.06.

To obtain insight regarding these results, we derived a theoretical model for the propagation of a single transition region in a multistable channel (Fig. 3). We considered a viscous fluid in a semi-infinite elastic channel with two stable cross-sectional shapes for given fluidic pressures p. For simplicity, and based on previous works such as refs. 25, 26, and 30, we adopted an approximated trilinear relation between the pressure induced by the internal flow and the channel cross-section. This approximation simplifies the relation between the fluidic pressure and the cross-sectional deformation to linear functions in both stable regions. This leads to a model of linearly elastic snapped-down channel at pressure below p_s^{up} and a model (with different geometric and physical parameters) of linearly elastic snapped-up channel at pressure above p_s^{down}. These two regions are then connected by an unstable branch, which is assumed to be linear as well. Combining these regions yields the trilinear relation. In addition, we assume that the channel length is much larger than the transition region separating between the two states. We thus consider the flow of a Newtonian incompressible fluid, governed by conservation of mass $\nabla \cdot \mathbf{u} = 0$, and, assuming negligible inertia, the Stokes equation is $\nabla p = \mu \nabla^2 \mathbf{u}$, where $\mathbf{u}$ is the velocity vector, p is pressure, and μ is the viscosity of the fluid. For flows in slender deformable channels, the mass-conservation equation can be integrated to take the following form:

$$w\frac{\partial \bar{h}}{\partial p}\frac{\partial p}{\partial t} + \frac{\partial q}{\partial x} = 0, \qquad [1]$$

where q is the volumetric flux in the x direction, w is the channel width, and $\bar{h}$ is the average height which represents a rectangular channel with identical cross-section area. Similarly, applying the standard lubrication approximation allows simplifying the Stokes equation to

$$q = -\frac{w\tilde{h}^3}{12\mu}\frac{\partial p}{\partial x}, \qquad [2]$$

where $\tilde{h}$ is the hydraulic height, representing the height of a rectangular channel which has identical viscous resistance to our unknown channel geometry. The value of $\tilde{h}$ is readily computed (here by using Abaqus) for both snapped-up and -down cross-sectional shapes. The cross-sectional area is given by $w\bar{h}(p) = a_i p + w\bar{h}_i$, where $\bar{h}_i$ are constants ($i = 1, 3$) representing the after and before snap-through cross-sectional areas for $p = 0$ (Fig. 2). Similarly, a trilinear relation is assumed for the

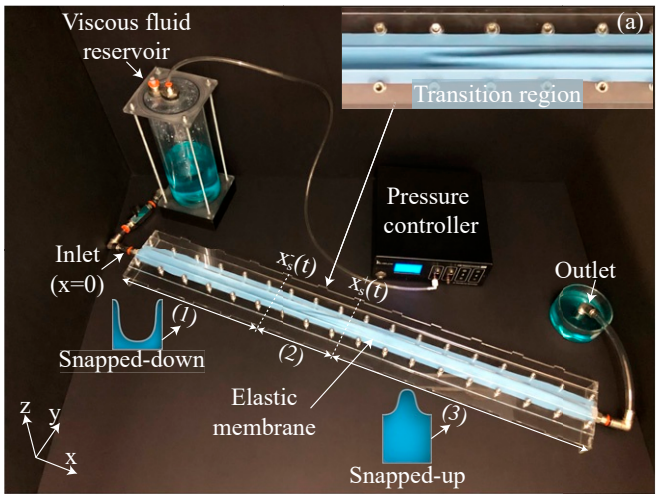

Fig. 2. Experimental setup. The pressure controller regulates a constant pressure at the viscous fluid reservoir, which is connected to the channel inlet via a flow valve. At the inlet ($x = 0$), negative gauge pressure is applied at $t = 0$, leading to snap-through of the elastic membrane between the snapped-down state (1) to the snapped-up state (3). Those two regions are separated by a transition region (2) that moves along the streamwise direction. The channel outlet is connected to another reservoir, which is opened to atmospheric pressure. A close-up view of the transition region is presented in *Inset (a)*.

Downloaded at Eyachar Central Lib Technion - Israel Inst of Tech on February 25, 2020

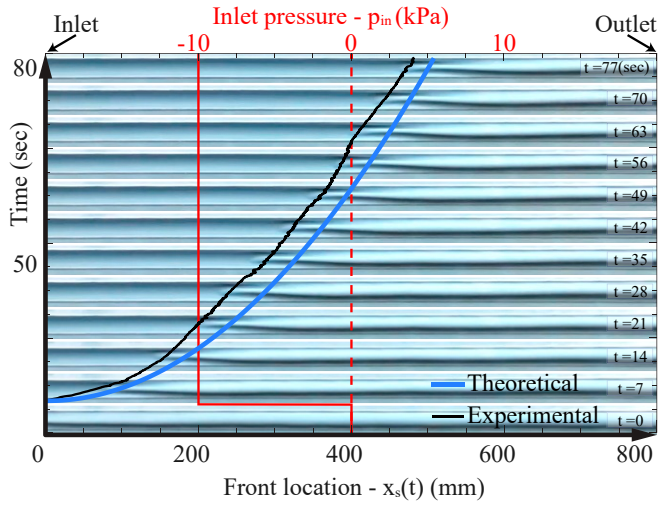

Fig. 3. Comparison between analytical and experimental results. Experimental and analytical results for a single transition-region propagation and the location of the transition region at different time intervals (from 0 to 80 s) and at varying inlet pressure (p_{in} 0 to −10 kPa) (red line, denoting inlet pressure) are shown (Movie S1).

channel viscous resistance, yielding $\tilde{h}^3(p) = b_i p + \tilde{h}_i^3$, where, in this case, $b_i p$ is neglected compared with the $\tilde{h}_i^3$ term. By substituting Eq. **2** into Eq. **1**, we get

$$a_i \frac{\partial p}{\partial t} = \frac{\tilde{h}_i^3}{12\mu} \frac{\partial}{\partial x}\left(\frac{\partial p_i}{\partial x}\right), \qquad [3]$$

where $i \in [1,3]$. The initial and boundary conditions are $p_1(x=0, t>0) = f(t)$, $p_3(x,0) = p_1(x,0) = 0$, $p_1(x_s^-, t) = p_3(x_s^+, t) = p_s$, and $p_3(x \to \infty, t) = 0$, where p_s is the snapping pressure (and may represent either p_s^{up} or p_s^{down}; Fig. 1). In addition to the above conditions, applying integral mass conservation on the transition region located at x_s, and limiting the configuration to sufficiently small transition region, yields the mass-conservation condition at the transition region

$$q(x_s^-) - (a_1 p_s + w\bar{h}_1)\frac{\partial x_s}{\partial t} = q(x_s^+) - (a_3 p_s + w\bar{h}_3)\frac{\partial x_s}{\partial t}. \qquad [4]$$

Substituting Eq. **2** into Eq. **4** yields

$$\left.\frac{\partial p_1}{\partial x}\right|_{x=x_s^-} - \frac{\tilde{h}_3^3}{\tilde{h}_1^3}\left.\frac{\partial p_3}{\partial x}\right|_{x=x_s^+} = \frac{\partial x_s}{\partial t}\kappa, \qquad [5]$$

which provides an additional condition for obtaining the location of the transition region $x_s(t)$, and where $\kappa = p_s(a_3 - a_1) + w(\bar{h}_3 - \bar{h}_1)$. The governing Eq. **3** are similar to one-dimensional heat transfer problem involving a phase change, known as the Stefan problem (31, 32). Integration and determining the integration coefficients by applying boundary and initial conditions yields the self-similar result of

$$p_1(x,t) = p_{in} + \frac{p_s - p_{in}}{\mathrm{erf}\,(\beta)}\mathrm{erf}\left(x\sqrt{\frac{3a_1\mu}{w\tilde{h}_1^3}t}\right), \qquad [6A]$$

$$p_3(x,t) = \frac{p_s}{1 - \mathrm{erf}\left(\beta\sqrt{\frac{\tilde{h}_1^3 a_3}{\tilde{h}_3^3 a_1}}\right)}\left[1 - \mathrm{erf}\left(x\sqrt{\frac{3a_3\mu}{w\tilde{h}_3^3}t}\right)\right], \qquad [6B]$$

where $x_s = \beta\sqrt{(3a_1\mu)/(w\tilde{h}_1^3)t}$ is the location of the transition region, and β is a constant still to be determined. To calculate β, the expressions obtained to the pressure in both regions Eq. **6** are substituted into Eq. **4**, yielding the additional relation

$$\frac{p_s - p_{in}}{\mathrm{erf}\,(\beta)}e^{-\beta^2} + \frac{e^{-\beta^2\frac{\tilde{h}_1^3 a_3}{\tilde{h}_3^3 a_1}}}{1 - \mathrm{erf}\left(\beta\sqrt{\frac{\tilde{h}_1^3 a_3}{\tilde{h}_3^3 a_1}}\right)}\sqrt{\frac{\tilde{h}_3^3 a_3}{\tilde{h}_1^3 a_1}}p_s + \beta\sqrt{\pi}\frac{\tilde{h}_1^3}{12a_1\mu}k = 0, \qquad [7]$$

(where κ is defined after Eq. **5**). While Eq. **7** is implicit in β, an approximate explicit solution can be obtained by regular asymptotic expansions (*SI Appendix*, section 1)

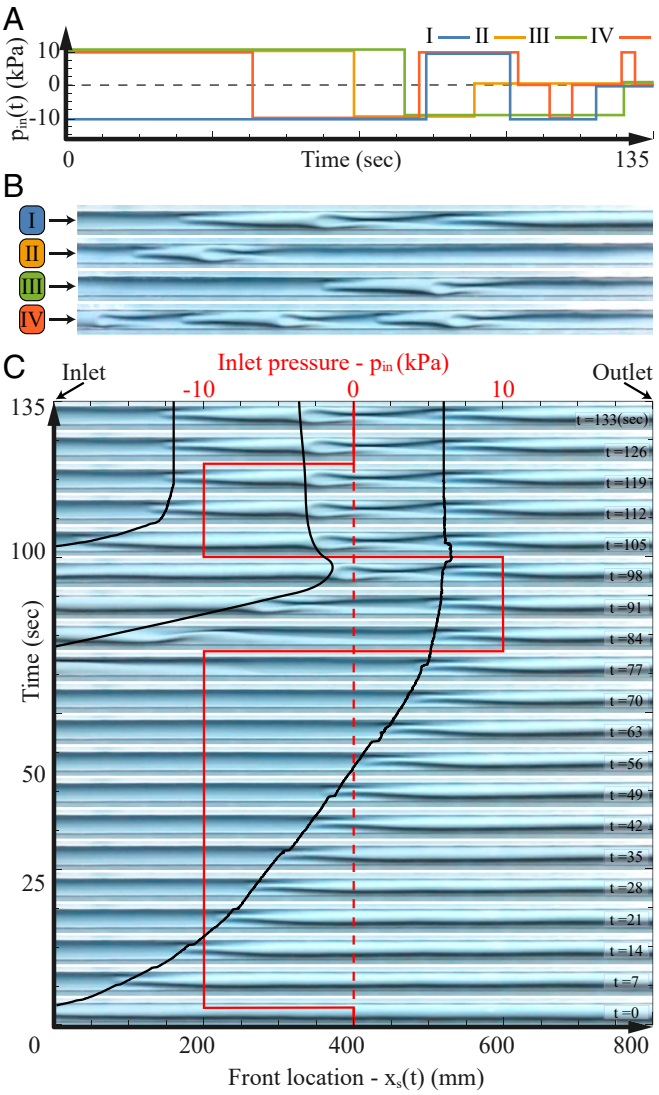

Fig. 4. Experimental results of patterning using multiple transition regions propagation. (*A* and *B*) *A* presents the inlet pressure profiles, and *B* presents the corresponding final steady deformation patterns. *C* presents the evolution of case a in *A*. Initially, the channel is at the snapped-up state. Then, we applied varying inlet pressures between negative- and positive-gauge values (red line; denoting inlet pressure) to generate moving snap-down and -up transition regions, which allow patterning of the continuously multistable membrane. After sequencing three transition regions (denoted by black line), separating four different stability states that are obtained, we removed pressure actuation, and the membrane pattern remained stable (t = 133 s) (Movie S1).

Downloaded at Eyachar Central Lib Technion - Israel Inst of Tech on February 25, 2020

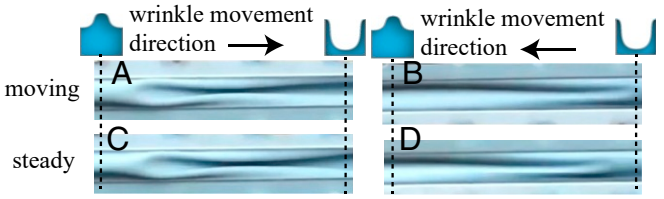

Fig. 5. Transient and static transition-region shapes. *A* and *B* present the moving snap-up and -down transition region, which are inverse of each other; *C* and *D* present the nearly unchanged shapes of the static transition region.

$$\beta_{asymptotic} \approx \sqrt{\frac{3a_1\mu}{\tilde{h}_1^3}\,(p_{in} - p_s)}, \qquad [8]$$

thus relating the motion of the transition region to the physical and geometrical parameters of the system. Calculation of β for the current configuration is presented in *SI Appendix*, section 2. As is evident in Fig. 3, a good agreement is observed between the estimated location of the transition region and the experimental results.

Above, we analytically analyzed and experimentally demonstrated the emergence and motion of a single transition region and showed that when the inlet pressure returns to its nominal value, the membrane's shape remains nearly unchanged. Thus, by sequencing several inlet pressures, any pattern of a snapped-down and -up regions along the channel can be created. The use of multiple moving transition regions for patterning is presented in Fig. 4. Fig. 4*A* presents various inlet pressure profiles, and the corresponding final patterns are presented in Fig. 4*B*. Fig. 4*C* focuses on the first pressure profile in Fig. 4*A* (marked by a blue line) and shows the temporal evolution of the patterning process. Initially, the channel is entirely at the snapped-up state. Then, we applied alternating positive- and negative-gauge inlet pressures (red line in Fig. 4, denoting inlet pressure) to generate moving snap-down and -up transition regions, thus patterning the equilibrium state of the continuously multistable membrane. Fig. 4 shows the evolution of the membrane shape and presents the location of the transition regions vs. time, as well as snapshots of the membrane shape at different time intervals.

We note that the shape of the transition regions, separating between the different cross-sectional equilibria states, resembles a single wrinkle (Fig. 5). Two possible geometric configurations of this wrinkle were observed and shown to be determined by the inducing flow field. In addition, some asymmetric wrinkles were occasionally observed, but were unstable and collapsed to the symmetric form (Fig. 4; at times $84 < t < 91$ [s]). A snap-down transition region, moving in the streamwise direction, is presented in Fig. 5*A*. A snap-up transition region is presented in Fig. 5*B*, which is similar to the inverse of the geometry presented in Fig. 5*A*. The transition-region shapes are nearly

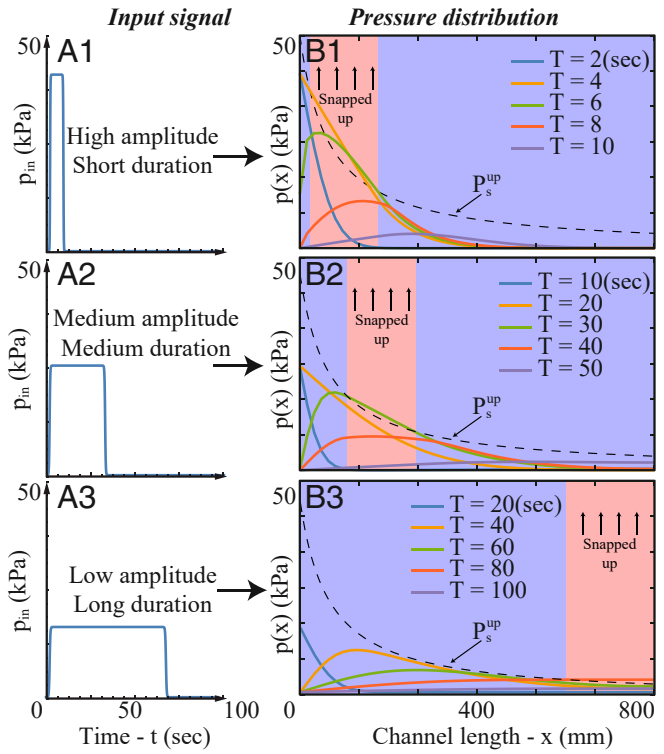

Fig. 6. Direct fluidic-induced patterning of any segment of a nonuniform membrane. Numerical solution of a membrane with spatially varying snapping pressure value is shown. (*A1–A3*) Three different inlet pressure actuations that vary in amplitude (A_{in}) and duration (Δt). (*B1–B3*) Pressure distribution vs. streamwise direction (x) for different times (full lines) along with snapping pressure distribution along the channel (p_s^{up}) (denoted by a dashed black line). Each case of actuation (1–3) snaps directly a different segment of the membrane (red background). The numerical code used is included in ref. 33.

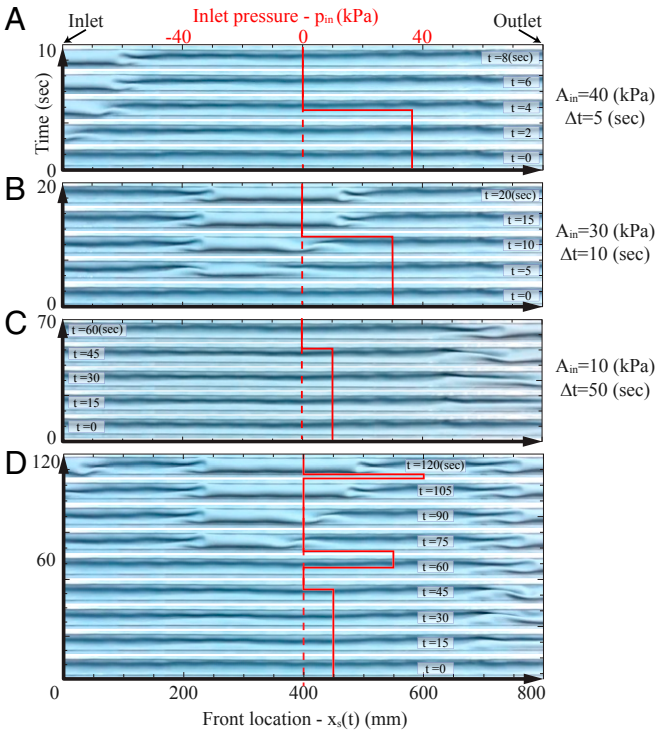

Fig. 7. Experimental results of direct fluidic-induced snapping of different regions of a nonuniform membrane. Different inlet signals are used to directly pattern different regions of a nonuniform membrane. The membrane thickness is spatially varying. At region $0 \le x \le 200$ mm, there are three layers of elastic membranes, yielding $p_s = 35$ kPa. At region $200 \le x \le 600$ mm, there are two layers, yielding $p_s = 15$ kPa. At the remainder of the membrane $600 < x < 800$ mm, there is a single layer, yielding $p_s = 5$ kPa. *A–C* present inlet signals with different amplitude and duration (A_{in}, Δt). In *A*, we apply high amplitude and short duration (40 kPa, 5 s), yielding a pressure field which snaps up only the three-layer region near the outlet. In *B*, we apply medium amplitude and medium duration (30 kPa, 10 s) and snap up the two-layer region in the middle of the channel. (*C*) We apply low amplitude and long duration (10 kPa, 50 s) and snap up the one-layer region near the outlet. *D* presents a combination of such signals to create a rather complex deformation pattern of the membrane. See Movie S2.

Downloaded at Eyachar Central Lib Technion - Israel Inst of Tech on February 25, 2020

unchanged after the ending of the fluidic driven actuation, as presented in Fig. 5 *C* and *D*.

So far, we examined only membranes with constant properties. Arbitrary patterning of such membranes required sequencing of several transition regions and waiting for all transition regions to reach the required positions. However, we can exploit the transient dynamics of the fluidic pressure, along with nonuniform membrane properties, to immediately snap up or snap down any segment of the membrane. This concept is illustrated in Fig. 6, which presents numerical solutions (see code in ref. 33) of the transient flow in contact with a membrane with continuously varying properties. In Fig. 6, the same set of Eq. **3** were solved. However, in this case, the snapping pressure spatially varied according to $p_s(x) = c_1/(x - c_2) + c_3$, and the inlet pressure was in the form of $p_{in}(t) = A_{in}(H[t] - H[t - \Delta t])$, where H is the Heaviside function. For $c_1 = 8.167$ kPa·m, $c_2 = 0.0817$ m, and $c_3 = -0.05$ kPa, Fig. 6 *A1–A3* presents three different inlet pressure signals that vary in amplitude A_{in} and duration Δt. Fig. 6 *B1–B3* presents the pressure field for different times (solid lines) along with snapping pressure distribution along the channel (p_s^{up}) (dashed black line). At regions where the fluidic pressure field surpasses the local value of the snapping pressure $p(x, t) > p_s^{up}(x)$, the structure will snap up (segments that snapped up are marked by a red background). We can see that the combination of actuation amplitude and duration determines the snapping region. Short duration with high amplitude actuates a segment near the inlet (case 1). Medium amplitude and medium duration actuates a segment in the middle (case 2). Low amplitude and long duration actuate a segment near the outlet (case 3). Thus, transient viscous dynamics allow us to directly initiate a snap-through in any segment of the membrane. By combining these different signals, and using the same principle with negative gauge pressures that initiate the snapping-down phenomenon, any desired pattern of the different equilibria states can be directly achieved.

In Fig. 7, we experimentally demonstrate this concept, using a membrane with piece-wise spatially varying snapping pressure. At region $0 \le x \le 200$ mm, there are three glued layers of elastic membranes, yielding $p_s = 35$ kPa. At region $200 \le x \le 600$ mm, there are two layers, yielding $p_s = 15$ kPa. At the remainder of the membrane ($600 \le x \le 800$ mm), there is a single layer, yielding $p_s = 5$ kPa. The direct actuation of each of these segments by varying the inlet pressure amplitude A_{in} and duration Δt is presented in Fig. 7 *A–C*. We show that $(A_{in}, \Delta t)$ of (40 kPa, 5 s) snap up the region near the inlet, while $(A_{in}, \Delta t)$ of (30 kPa, 10 s) snap up the region in the middle of the channel, and $(A_{in}, \Delta t)$ of (10 kPa, 50 s) snap up the region near the outlet. The snapping-pressure measurements were based on averaging six experiments and used air actuation to ensure elimination of transient fluidic effects, yielding SD under ± 1.3 kPa in all cases. Finally, in Fig. 7*D*, we demonstrate the combination of such signals to create a rather complex deformation pattern of the membrane. The effects of the membrane geometry on the snapping pressure are discussed in *SI Appendix*, Fig. S4 and section 3.

To conclude, in this work, we addressed the challenge of underactuated control of continuous multistable structures, which could play a vital role in the fields of soft robotics, MEMS, and meta-materials. We focused our study on a simple illustrative configuration composed of an slender elastic membrane, which is actuated by a viscous fluid. The membrane is able to concurrently sustain two different modes of stable cross-section shapes at different segments of the membrane. These different segments are shown to be separated by transition regions, and the location of these regions sets the stable equilibrium shape of the membrane. We theoretically analyzed and experimentally demonstrated the formation and motion of a single, and multiple, transition regions due to manipulation of the fluidic inlet pressure. We showed that sequencing of multiple transition regions enables one to achieve underactuated control of the membrane equilibria shape.

Detailed descriptions appear in *SI Appendix*, and related codes used in the work are available at Figshare, https://doi.org/10.6084/m9.figshare.11648022.v1.

1. S. D. Guest, S. Pellegrino, Analytical models for bistable cylindrical shells. *Proc. R. Soc. A*, **462**, 839–854 (2006).
2. K. Seffen, "Bi-stable concepts for reconfigurable structures" in *45th AIAA/ASME/ASCE/AHS/ASC Structures, Structural Dynamics & Materials Conference* (American Institute of Aeronautics and Astronautics, Reston, VA, 2004), p. 1526.
3. M. Follador, A. T. Conn, J. Rossiter, Bistable minimum energy structures (BiMES) for binary robotics. *Smart Mater. Struct.*, **24**, 065037 2015.
4. H. Rodrigue, W. Wang, M.-W. Han, T. J. Y. Kim, S.-H. Ahn, An overview of shape memory alloy-coupled actuators and robots. *Soft Robot.*, **4**, 3–15 (2017).
5. B. Treml, A. Gillman, P. Buskohl, R. Vaia, Origami mechanologic. *Proc. Natl. Acad. Sci. U.S.A.* **115**, 6916–6921 (2018).
6. J. B. Grotberg, O. E. Jensen, Biofluid mechanics in flexible tubes. *Annu. Rev. Fluid Mech.*, **36**, 121–147 (2004).
7. J. R. Lister, Buoyancy-driven fluid fracture: The effects of material toughness and of low-viscosity precursors. *J. Fluid Mech.* **210**, 263–280 (1990).
8. B. Mosadegh *et al.*, Pneumatic networks for soft robotics that actuate rapidly. *Adv. Funct. Mater.* **24**, 2163–2170 (2014).
9. Y. Matia, A. D. Gat, Dynamics of elastic beams with embedded fluid-filled parallel-channel networks. *Soft Robot.* **2**, 42–47 (2015).
10. D. Chakraborty, J. R. Prakash, J. Friend, L. Yeo, Fluid-structure interaction in deformable microchannels. *Phys. Fluids* **24**, 102002 (2012).
11. S. Rubin, A. Tulchinsky, A. D. Gat, M. Bercovici, Elastic deformations driven by non-uniform lubrication flows. *J. Fluid Mech.* **812**, 841–865 (2017).
12. I. C. Christov, V. Cognet, T. C. Shidhore, H. A. Stone, Flow rate–pressure drop relation for deformable shallow microfluidic channels. *J. Fluid Mech.*, **841**, 267–286 (2018).
13. C. Duprat, H. A. Stone, *Fluid-Structure Interactions in Low-Reynolds-Number Flows* (Royal Society of Chemistry, London, 2015).
14. D. Glozman, N. Hassidov, M. Senesh, M. Shoham, A self-propelled inflatable earthworm-like endoscope actuated by single supply line. *IEEE Trans. Biomed. Eng.* **57**, 1264–1272 (2010).
15. M. Heil, A. L. Hazel, Fluid-structure interaction in internal physiological flows. *Annu. Rev. Fluid Mech.* **43**, 141–162 (2011).
16. M. Heil, Stokes flow in collapsible tubes: Computation and experiment. *J. Fluid Mech.* **353**, 285–312 (1997).
17. M. Gomez, D. E. Moulton, D. Vella, Passive control of viscous flow via elastic snap-through. *Phys. Rev. Lett.* **119**, 144502 (2017).
18. E. Ben-Haim, L. Salem, Y. Or, A. D. Gat, Single-input control of multiple fluid-driven elastic actuators via interaction between bi-stability and viscosity. arXiv:1903.04280 (6 March 2019).
19. A. L. Hazel, M. Heil, Steady finite-Reynolds-number flows in three-dimensional collapsible tubes. *J. Fluid Mech.* **486**, 79–103 (2003).
20. G. Arena *et al.*, Adaptive compliant structures for flow regulation. *Proc. R. Soc. A* **473**, 20170334 (2017).
21. Z. Zhakypov, K. Mori, K. Hosoda, J. Paik, Designing minimal and scalable insect-inspired multi-locomotion millirobots. *Nature* **571**, 381–386 (2019).
22. J. Vandermarlière, On the inflation of a rubber balloon. *Phys. Teach.* **54**, 566–567 (2016).
23. G. Puglisi, L. Truskinovsky, Mechanics of a discrete chain with bi-stable elements. *J. Mech. Phys. Solid.* **48**, 1–27 (2000).
24. W. Dreyer, I. Müller, P. Strehlow, A study of equilibria of interconnected balloons. *Q. J. Mech. Appl. Math.* **35**, 419–440 (1982).
25. T. Cohen, S. Givli, Dynamics of a discrete chain of bi-stable elements: A biomimetic shock absorbing mechanism. *J. Mech. Phys. Solid.* **64**, 426–439 (2014).
26. I. Benichou, E. Faran, D. Shilo, S. Givli, Application of a bi-stable chain model for the analysis of jerky twin boundary motion in NiMnGa. *Appl. Phys. Lett.*, **102**, 011912 (2013).
27. B. Gorissen *et al.*, Hardware sequencing of inflatable nonlinear actuators for autonomous soft robots. *Adv. Mater.* **31**, 1804598 (2019).
28. L. Hines, K. Petersen, M. Sitti, Inflated soft actuators with reversible stable deformations. *Adv. Mater.* **28**, 3690–3696 (2016).
29. Y. Fei, W. Pang, Analysis on nonlinear turning motion of multi-spherical soft robots. *Nonlinear Dyn.* **88**, 883–892 (2017).
30. A. Luongo, S. Casciati, D. Zulli, Perturbation method for the dynamic analysis of a bistable oscillator under slow harmonic excitation. *Smart Struct. Syst.* **18**, 183–196 (2016).
31. L. I. Rubinstein, *The Stefan Problem* (American Mathematical Society, Providence, RI, 2000), vol. 8.
32. L. G. Leal, *Advanced Transport Phenomena: Fluid Mechanics and Convective Transport Processes* (Cambridge University Press, Cambridge, UK, 2007), vol. 7.
33. O. Peretz, A. K. Mishra, R. F. Shepherd, A. D. Gat, Underactuated fluidic control of a continuous multistable membrane - Mathematica code. Figshare. https://doi.org/10.6084/m9.figshare.11648022.v1. Deposited 18 January 2020.

Downloaded at Eyachar Central Lib Technion - Israel Inst of Tech on February 25, 2020